IEEE Access
Multidisciplinary ⋮ Rapid Review ⋮ Open Access Journal

Received 27 April 2023, accepted 22 May 2023, date of publication 29 May 2023, date of current version 1 June 2023.

Digital Object Identifier 10.1109/ACCESS.2023.3280422

RESEARCH ARTICLE

Multi-Input Deep Learning Approach for Breast Cancer Screening Using Thermal Infrared Imaging and Clinical Data

DENNIES TSIETSO[1], (Student Member, IEEE), ABID YAHYA[1], (Senior Member, IEEE), RAVI SAMIKANNU[1], (Senior Member, IEEE), MUHAMMAD USMAN TARIQ[2], (Member, IEEE), MUHAMMAD BABAR[3], (Member, IEEE), BASIT QURESHI[4], (Senior Member, IEEE), AND ANIS KOUBAA[3], (Senior Member, IEEE)

[1]Department of Electrical, Computer and Telecommunications Engineering, Botswana International University of Science and Technology, Palapye, Botswana
[2]Department of Marketing, Operations, and Information Systems, Abu Dhabi University, Abu Dhabi, United Arab Emirates
[3]Robotics and Internet of Things Laboratory, Prince Sultan University, Riyadh 11586, Saudi Arabia
[4]College of Computer and Information Sciences, Prince Sultan University, Riyadh 11586, Saudi Arabia

Corresponding author: Dennies Tsietso (dennies.tsietso@studentmail.biust.ac.bw)

This work was supported in part by Prince Sultan University, Saudi Arabia, under Grant SEED-CCIS-2023-121.

ABSTRACT Breast cancer is one of the most prevalent causes of death among women across the globe. Early detection is the best strategy for reducing the mortality rate. Currently, mammography is the standard screening modality, which has its shortcomings. To complement this modality, thermal infrared-based Computer-Aided Diagnosis (CADx) tools have been presented as economical, less hazardous, and a suitable solution for various age groups. Although a viable solution, most CADx systems are built primarily from frontal breast thermograms, and are likely to miss lesions that may develop on the sides. Additionally, these systems often disregard critical clinical data, such as risk factors. This paper presents a novel CADx system that utilizes deep learning techniques for breast cancer detection. The system incorporates multiple breast thermogram views and corresponding patient clinical data to improve the accuracy of the diagnosis. We describe the methodology of the system, including the extraction of regions of interest from images and the use of transfer learning to train three different models. We evaluate the performance of the models and compare them to similar works from the literature. The results demonstrate that using multi-inputs outperforms single-input models and achieves an overall accuracy of 90.48%, a sensitivity of 93.33%, and an AUROC curve of 0.94. This approach could offer a more cost-effective and less hazardous screening option for breast cancer detection, particularly for a wide range of age groups.

INDEX TERMS Breast cancer, CADx, deep learning, segmentation, thermography, transfer learning.

I. INTRODUCTION

Breast cancer is one of the women's most lethal forms of cancer. In 2020, nearly 2.3 million new instances of breast cancer were registered by the Global Cancer Observatory, for which it was typified as the second leading cause of death in women [1]. As opposed to developed countries, most mortalities occur in developing countries [2]. Nevertheless, the incidence rate per 100,000 women was higher in developed countries than in developing countries [3]. This can be attributed to a greater reporting of incidence in the community with higher income levels in all age groups [2]. The burden of high mortality rates in developing countries is attributed to poor breast cancer awareness campaigns and poor health infrastructures that lack adequate screening resources for early detection and adequate clinical treatment [4], [5].

An early breast cancer diagnosis can reduce treatment costs and promote prompt treatment, thereby improving chances for survival [6]. This view is supported by Nickson et al. [7], who points out that the survival rate from breast cancer

The associate editor coordinating the review of this manuscript and approving it for publication was Luca Cassano.

is highly associated with the size of the tumor when it is detected at usually less than 10mm, with the patients having a 98% chance of survival. This fact has motivated researchers to devote their attention to developing Computer Aided Diagnosis (CADx) systems for early and accurate detection, thus improving the survival chances for patients. Also, an efficient CADx system can minimize the pathologist's workload and mitigate the level of subjectivity in disease diagnosis. [8]. Mammography is considered the gold standard for early detection. However, it is an invasive modality that causes discomfort and employs ionizing radiation, which has a radiation-induced breast cancer risk [9]. Furthermore, it is not advisable for young women due to the low contrast caused by thick breast tissue common in this age group [10]. Moreover, it is infeasible for large-scale screening in developing countries, where it can be cost-ineffective [11]. Thermography is another technique that deserves more research attention to complement other screening modalities. It is exceptionally low-cost, well-suited for dense breasts, a non-invasive approach, and radiation hazard-free, thus posing zero risk to patients [12], [13], [14], [15].

Deep learning methods, particularly Deep Neural Networks (DNNs), are widely adopted for classification tasks in various fields due to their exceptional performance. In computer vision, Convolutional Neural Networks (CNNs), for example, have revolutionized image recognition tasks and surpassed human-level performance in some cases. Their effectiveness in computer vision stems from their unique working principle, which is inspired by the brain's visual cortex. Specifically, the visual cortex analyzes sensory nerve impulses from the eyes [16], with neurons responding to specific visual field patterns known as the receptive field, as discovered by Hubel and Wiesel [17]. Therefore, many DNNs for visual tasks are derived from CNNs. In clinical radiology, DNNs are being adopted for several tasks such as segmentation, detection, and more. One significant benefit of using DNNs in clinical workflows is their ability to handle large and complex datasets, which is essential for accurate and reliable diagnosis. Moreover, transfer learning has become an integral part of the DNN training process. This concept is based on the fact that humans can use previously acquired knowledge to tackle new problems. Inspired by this, transfer learning adopts a similar approach. It involves leveraging existing knowledge from pre-trained models to facilitate training in a new, related task. These pre-trained models have been trained on large and diverse datasets and learned highly discriminative features useful for a wide range of image classification tasks. By reusing pre-trained models, we can reduce the computational cost and training time required for a new task and achieve improved performance [18], especially in the medical domain where large, diverse datasets are scarce.

The majority of CADx systems based on thermography in the literature primarily focus on frontal breast thermograms and may overlook lesions present on the sides. Moreover, these systems often neglect the integration of intrinsic clinical data, despite its potential to significantly improve their performance. To address these limitations, CADx systems must consider incorporating both lateral breast thermograms and patient clinical data, which comprises risk factors related to breast cancer, for improved coverage and performance. For efficient symmetry analysis and reduced computational requirements for the learning algorithm, the use of segmentation is necessary to extract the Region of Interest (ROI) from which features will be derived from a reduced feature set. This study presents a method for classifying multi-views of breast thermograms and corresponding patient clinical data as either healthy or unhealthy. This was accomplished by building a multi-input network and incorporating transfer learning by adopting pre-trained layers of a DNN. The network takes in two forms of data: clinical data and three different views of the breast obtained through the Static Infrared Thermography (SIT) protocol. It further presents a method for automatic ROI extraction. The study also designed a graphical user interface (GUI) to simulate the model. The contributions are aggregated as follows:

- Integration of transfer learning to improve efficiency and reduce computational costs
- Development of a multi-input network that incorporates clinical data and three breast views for accurate classification of healthy/unhealthy patients
- Introduction of a method for automatic ROI extraction for efficient symmetry analysis

The article is organized as follows: Section II describes the related works in breast cancer diagnosis; Section III explains the methods and the data set; Section IV presents the experimental results; we discuss these results in Section V; finally, the conclusions are drawn in Section VI.

II. RELATED WORK

Mambou et al. [19] proposed a CAD system based on a DNN coupled with a Support Vector Machine (SVM) classifier for detecting breast cancer from thermal infrared images. They utilized a pre-trained Inception V3 model and altered its last fully connected layer to create a binary classifier. An SVM classifier was then coupled to handle situations of uncertainty in the DNN's output. The study used frontal breast thermograms acquired through the Dynamic Infrared Thermography (DIT) protocol, which involves taking pictures after thermal stimulation of the breast area. The ROI was manually extracted and transformed into a matrix of features to be processed by the network. It would have been more interesting to automate the segmentation process to make the CADx system more practical. Overall, delegating the processing of the feature matrix to the SVM when the DNN had a confidence level of <0.6 and ≥ 0.5 is a remarkable feature that could serve as robustness against misclassifications.

In [20], a method was presented that utilizes the pre-trained DenseNet121 as a feature extractor to build a classifier for frontal breast thermograms. First, they converted the original image into a three-channel edge-prominent image using the Roberts and Prewitt edge detectors. The rationale behind this

operation was to extract edge information that details possible deformations on the breasts and combine these edges with the original image to have rich information. They further compared the performance of their model with other state-of-the-art models and found that it outperformed them with an accuracy of 98.80% and 99.00% precision. The authors conceded to data and computational power limitations but resolved these through transfer learning, which accommodates small datasets and speeds up training. To determine the optimal number of epochs for their model, they used six other pre-trained models to identify the number of epochs when the model began to overfit the data. An optimization technique could have been used as an alternative process, which has been effectively implemented in a comparable investigation by Elkorany et al. [21].

Sanchez et al. [22] proposed a method that combines multi-views of breast thermograms with personal and clinical data. The images were acquired via the SIT method, with lateral views acquired at a 90-degree angle. Their model achieved a classification accuracy of 97%. The authors found that incorporating frontal and lateral views and clinical data aided in building a model with results that were similar or even better compared to those found in the literature. Furthermore, they suggested that the image segmentation stage could be avoided by acquiring more information from patients. Firstly, adding lateral views of breast thermograms to the front view improves the model's accuracy. Secondly, incorporating the clinical and personal data helps detect sick patients, therefore reducing the number of false negatives and increasing the model's sensitivity. Nevertheless, the authors did plan to explore the effects of segmentation in their future work, a recommendation that we fully agree with. One limitation of their study was the significant imbalance between the classes of the dataset used and the presence of numerous noisy images encountered during data preparation.

In [23], the authors presented a technique in which textural features from multi-view breast thermograms are fused and used to train an SVM classifier. The level-set method was adopted for segmenting lateral breast thermograms. Next, Gray-Level Co-occurrence Matrix features were extracted from frontal and lateral ROIs. They then carried out a two-step feature reduction process. First, the t-test statistical test was used to consider features for which $p \leq 0.0001$. Finally, the Kernel Principal Component Analysis was employed to obtain significant features. Six features were found to be significant from frontal and right-side views, whereas four were for left-side views. These features were then fused to create a composite feature vector to train a least-squares SVM. The use of fused texture features resulted in an accuracy of 96%, specificity of 92%, and a sensitivity of 100%. However, this work does not report any results on the performance of the proposed segmentation method.

A study by Tiwari et al. [24] used a unique approach to classify breast thermograms. The study used SIT and DIT-acquired thermograms to train a pre-trained VGG-16 model. The preprocessing stage involved merging the frontal, left, and right view thermograms into a single image they refer to as a "multi-view image." These images were then augmented to increase the size of the dataset. The same dataset was used to train the ResNet-50-V2, Inception-V3, and VGG-19 models for comparison. The results showed that the VGG-16 model achieved the highest training, validation, and testing accuracy on SIT and DIT acquired images compared to its counterparts. In their concluding remarks, the authors note that the concatenation of multi-view breast thermal images delivers high accuracy as more information is fed into the classifier. Based on these results, we recommend concatenating segmented ROIs for improved accuracy.

In [25], a CNN was trained using various angles of breast thermograms. The study employed five different views of breast thermograms (i.e., front, left 45°, right 45°, left 90°, and right 90°). The authors built a separate CNN for each angle and trained it independently to determine the best individual models before combining their output. Then, they incorporated personal and clinical data to evaluate the impact on the model's performance. The results showed that adding clinical data significantly improved the model's accuracy, from 85.4% without clinical data to 93.8% with clinical data. The authors conclude by considering segmentation and transfer learning as future avenues, which we fully agree with.

In light of the reviewed works, this paper employs transfer learning to develop a predictive model instead of the traditional method of training from scratch, as seen in previous studies. The study also includes clinical data as an input to the model, whereas previous studies have mostly relied solely on thermograms. Additionally, this study uses automatic segmentation on both frontal and lateral view breast thermograms, whereas previous studies have either not performed segmentation or have limited it to only the frontal view. To highlight the potential application of this work, a GUI was developed to simulate the screening process, a feature not commonly seen in other studies.

III. MATERIALS AND METHODS

This section provides a detailed account of the methodology employed to design a deep learning-based CADx system that seamlessly integrates multi-view breast thermograms and personal and clinical data of patients, as depicted in Fig. 1. The methodology follows a multi-stage process that commences with data acquisition, where we collate a dataset of multi-view breast thermograms and patients' personal and clinical data. The collected data undergoes preprocessing, where relevant personal and clinical features are selected and processed, and the ROI is automatically segmented from each breast thermogram. Furthermore, we employ data augmentation techniques to expand the dataset's size. In the subsequent stage of model development, we utilize a pre-trained DNN architecture, namely AlexNet, to extract salient features from each extracted ROI of the breast thermograms, while a separate Neural Network (NN) processes the clinical and personal features. These features are subsequently merged to create a single network that offers a comprehensive analysis.

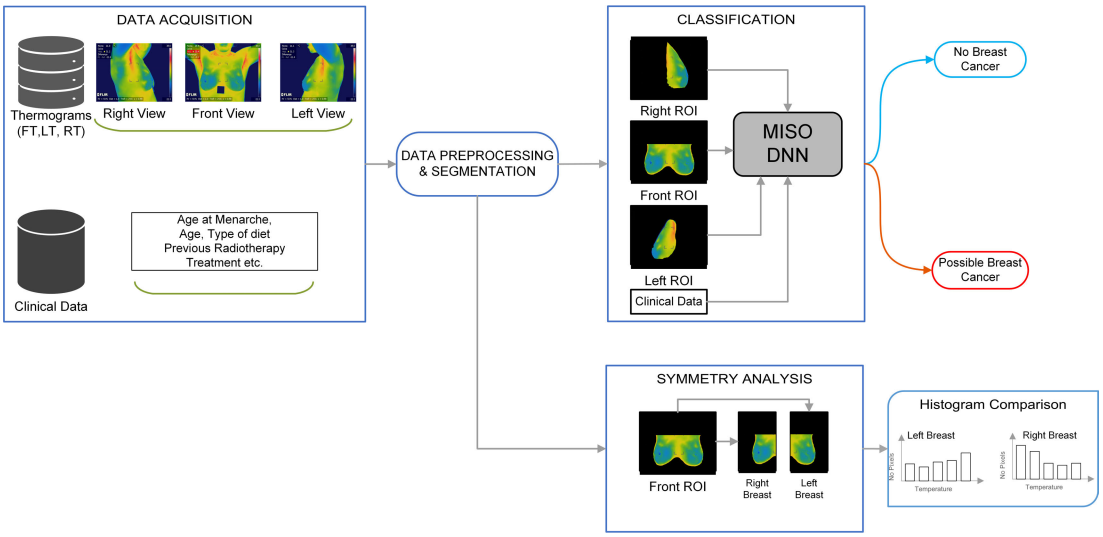

FIGURE 1. Overview of the proposed screening method. Thermograms adapted from [26].

We develop a GUI to demonstrate the system's functionality. Ultimately, the system's performance is evaluated utilizing various metrics and compared with related works to evaluate its potential in aiding radiologists in detecting early indications of breast cancer and improving diagnostic accuracy. The system's key components are presented in Fig. 2.

A. DATA ACQUISITION

This study utilized the breast thermograms from the DMR database, which were obtained by the Federal Fluminense University from volunteers in Brazil [26]. The dataset is publicly accessible for research purposes, and its collection was ethically approved. It hosts thermal infrared images captured at various views of the breast using the SIT and DIT protocols. The images were taken with an FLIR SC-620 thermal infrared camera with a resolution of 640 × 480 pixels and a thermal sensitivity of $40mK$. In the SIT protocol, a single image was taken per patient at five different angles: frontal and lateral views at 90° and 45°, whereas in the DIT protocol, a series of images were captured over time. This work used a sample of 101 breast thermograms (75 normal, 26 abnormal) captured via the SIT protocol. The database also includes the corresponding patients' clinical information. Table. 1 summarizes this dataset.

B. DATA PREPROCESSING

Data preprocessing is a crucial step in the analysis of breast thermograms and the application of machine learning techniques. This stage entails the preparation of data for subsequent analysis through cleaning, transformation, and organization to enhance the accuracy and efficiency of subsequent processes.

1) PREPROCESSING OF BREAST THERMOGRAMS

Exams with missing thermograms for any view and those with amputated breasts were not included in the dataset.

TABLE 1. Overview of the dataset used in the study.

Data	Format	Characteristics
Breast Thermograms	JPEG	multi-view (Front, Left-90° Right-90°); True-color; 640 × 480 resolution; SIT Protocol
Patient Personal and Clinical Data	Tabular Data	Risk factors, Complementary features, and Protocol features

Likewise, blurry images were also removed from the cohort. The acquired thermograms are low resolution images with unclear boundaries. Therefore, prior to segmentation, the thermograms were subjected to preprocessing tasks including conversion to grey scale and image enhancement obtained through various filters detailed in the subsequent section.

2) PREPROCESSING OF CLINICAL DATA

As explained in [22], the clinical and personal data in the database can be classified into three categories: risk factors, complementary features, and protocol features. The complementary features encompass mastectomy, prosthesis presence, nipple alterations, and the presence of breast warts. The features of the protocol encompass pre-examination activities such as smoking, coffee consumption, alcohol intake, physical exercise, and the application of deodorant or similar products on the breasts or underarms. The clinical data was filtered to only include the features deemed risk factors based on domain knowledge regarding their correlation with breast cancer, as depicted in Table. 2. In addition to these risk factors, temperature was deemed a crucial feature. Other preprocessing tasks applied to clinical data encompass normalization of numerical features, encoding of categorical features, and filling the missing fields. However, any instances with persistently missing fields were disregarded.

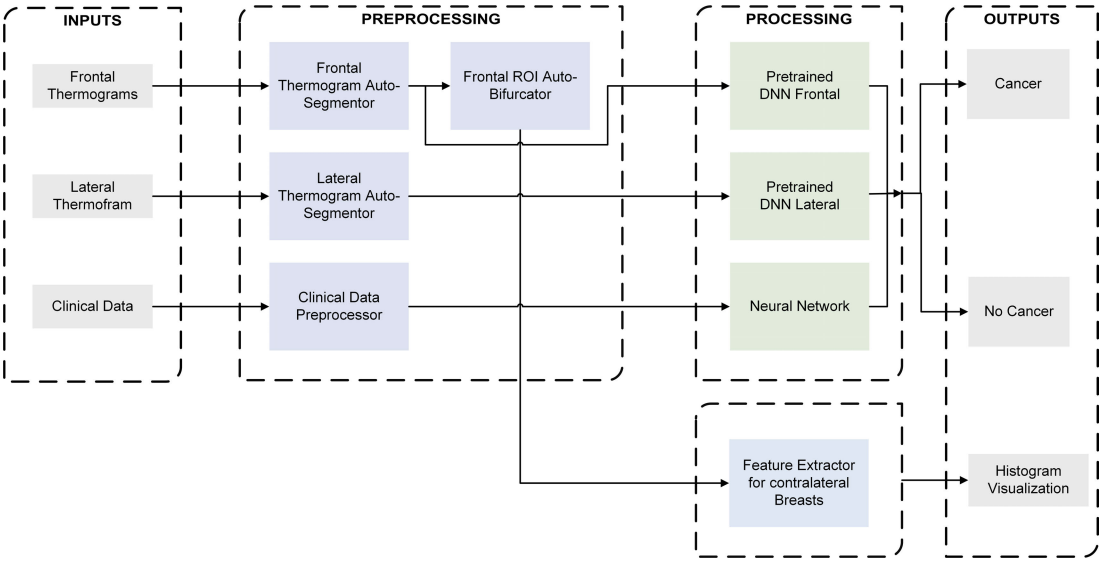

FIGURE 2. Architecture for the predictive model.

TABLE 2. Features selected as significant risk factors for breast cancer and elucidation of their impact on the disease.

Feature	Correlation
Age	The risk increases with age [27]
Age at menarche	An earlier age at menarche is a risk factor since it elevates susceptibility to breast carcinogenesis. [28]
Last Menstrual Period	Women who experience late-onset menopause (i.e., when they're older than 55) are at risk of breast cancer [29] [30]
Eating habits	According to [31], a fatty diet increases the risk of breast cancer. This occurs due to the surplus fat cells producing estrogen, leading to an increase in breast cell growth. This results in dense breasts, which is a known risk factor.
Radiotherapy?	Exposure to ionizing radiation has risk for subsequent breast cancer [32]
Use of Hormone Replacement?	The risk of having breast cancer diagnosed is increased in women using HRT and increases with longer duration of use [33]

C. SEGMENTATION

Segmentation is critical to ensuring the model focuses on the most relevant information in the breast thermograms and ignores irrelevant or noisy areas, ultimately enhancing the system's performance. Conventionally, images are segmented manually to extract the ROI, after which they are used to train a learning algorithm. The drawback of this approach is that it is tedious. In this study, segmentation was automated. A CADx system that employs automated ROI extraction facilitates mass screening. Moreover, it ensures consistency and reduces the risk of inter-observer variability. The approach for segmenting frontal and lateral breast thermograms is discussed in detail in the following subsections.

1) SEGMENTATION OF FRONTAL BREAST THERMOGRAMS

Although the frontal view thermogram has more features, it is harder to segment, so multiple techniques were combined to extract the ROI. The approach illustrated in Fig. 3 was used to extract the frontal ROI. Initially, as already discussed in III-B, a thermogram was converted into a grayscale image I_{grey}, followed by denoising through the application of anisotropic diffusion and a Gaussian kernel defined in (1),

$$G_\sigma(x,y) = \frac{1}{2\pi\sigma^2}\exp\left(-\frac{x^2+y^2}{2\sigma^2}\right) \tag{1}$$

where σ is the standard deviation of the Gaussian kernel and x and y are the respective distances to the horizontal and vertical centers of the kernel. The Gaussian filtering process was carried out by convolving the image with a 2D Gaussian filter, using a standard deviation of $\sigma = 1.618$. Edges were detected using the Canny edge detector. Given the grayscale image I_{grey}, gradient images were first produced by convolving I_{grey} with edge operators as defined in (2) and (3).

$$G_x = I_{grey} \circledast \Delta_x \tag{2}$$

$$G_y = I_{grey} \circledast \Delta_y \tag{3}$$

where Δ_y and Δ_x are the vertical and horizontal edge operators, respectively. The edge strength is then approximated at each pixel by computing the gradient magnitude, as shown in (4)

$$G = \sqrt{G_x + G_y} \tag{4}$$

Finally we obtain the edge image I_{edges} guided by threshold α using (5).

$$I_{edge}(x,y) = \begin{cases} 1: & G(x,y) \geq \alpha \\ 0: & otherwise \end{cases} \tag{5}$$

In this study, a threshold of $\alpha = 0.2333$ was used. Afterwards, a series of morphological operations were performed to connect disconnected boundaries and enhance edges.

All the frontal thermograms were tagged during acquisition; as such, a square object representing this tag was filtered out through an Euler number or characteristic. This image topological feature defines the total number of objects in

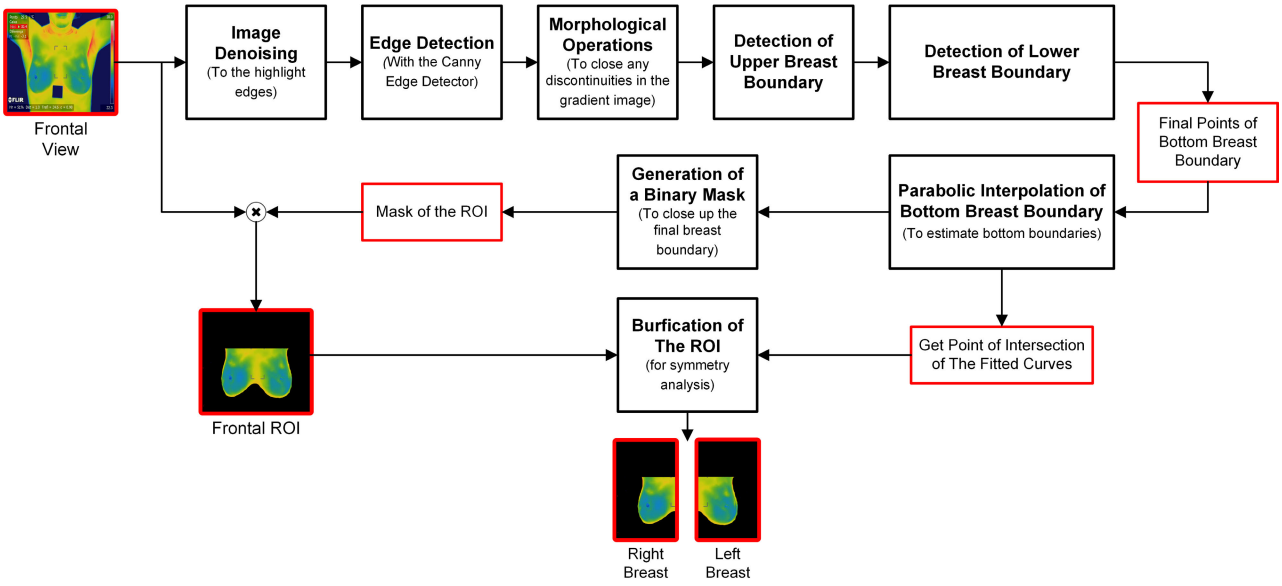

FIGURE 3. Block diagram of frontal breast thermogram segmentation method. Thermogram adapted from [26].

an image minus the total of those with holes. This implied that only objects without holes (i.e., with an Euler number equal to one) were retained. Female anatomy has concavity and convexity along the breast boundary (i.e., anterior axillary line), which were leveraged for tracing the lateral and upper boundaries. As shown in Fig. 4(a), the points $C1$ and $C2$ define the convex points of the outer breast boundary. Tracing edges column-wise from the first column, the first instance with white pixels between the first and last dark pixel delineates the convex point $C1$. A similar approach was performed for $C2$, starting at the end. These points were then used to determine the upper boundary. The next step involved identifying points for the infra-mammary line of the bottom breast region, which were then fitted to second degree polynomials P_{left} and P_{right} to estimate the complete bottom boundary, as shown in Fig. 4(b). Finally, the intersection of these curves (r_{inter}, c_{inter}) was used as the reference for segmenting the frontal ROI into the left and right breast. The process for frontal ROI extraction is summarized in 1.

2) SEGMENTATION OF LATERAL BREAST THERMOGRAMS

As depicted in Fig. 4; the initial steps for lateral thermogram segmentation are similar to those for the frontal thermogram. The same denoising filters tuned to the same parameters were used, and edges were detected using the same techniques. However, the first distinction lies in determining the upper and left boundaries (for the right breast). Due to the image acquisition protocol, the neck is present in almost all thermograms. As such, this was leveraged for filtering out the unwanted area. On Fig. 4(a), the row r_n and column c_n of the convex point formed by the neck and chest area were used to represent the corner formed by the upper and left boundaries of the breast region. A similar approach was adopted for estimating the complete bottom breast boundary by fitting a second-degree polynomial P to the bottom boundary points, as seen in Fig. 4(b). To preserve the breast region, the left boundary was rotated about point (r_n, c_n) using Euler angles and a rotation matrix. Finally, the intersection of the newly rotated left boundary with the curve P was used to slice out the breast region from the unwanted area. This procedure is summarized in 2 for the right breast and vice versa for the left side.

D. DATA AUGMENTATION

As already discussed in III-A, the sample used in this study is too small and has a class imbalance. Imbalanced data is a common issue in real-world settings that can impede the performance of learning algorithms [34]. As noted by Fang et al. [35], one of the primary causes of overfitting is the limited number of training instances and the use of inadequate features in the models for the given task. A small dataset can increase the risk of overfitting, which can in turn hinder the model's performance. To address this, data augmentation will be employed in the preprocessing pipeline of training data. Three common random transformations: vertical flip, horizontal flip, rotation, and scaling will be used on the training set, and the range of each transformation is summarized in Table. 3. These transformations will be applied on the ROIs set for training.

E. CLASSIFICATION

This study will use a deep learning-based predictive model to classify the segmented ROIs and clinical data as healthy and unhealthy. A multi-input, single-output network will be constructed in which each input is processed by its own sub-network. The outputs of these sub-networks will be combined to form a single output representing the final prediction of the model. This approach will allow the model to take advantage of the complementary information provided by different forms of data, leading to improved performance

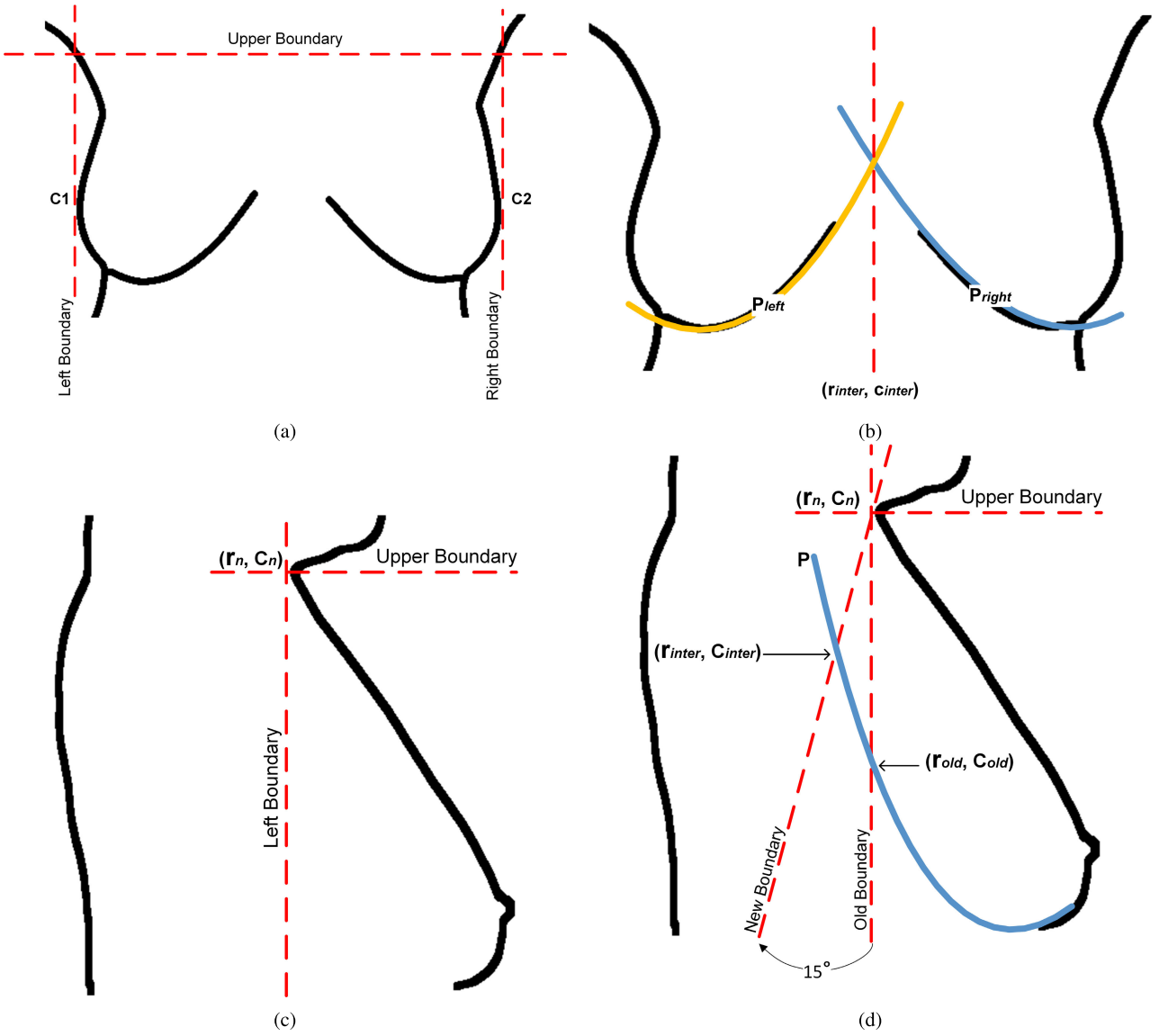

FIGURE 4. The segmentation method. (a) Lateral and upper boundaries. (b) Estimation of bottom boundary. (c) Left and upper boundaries. (d) Estimation of bottom boundary.

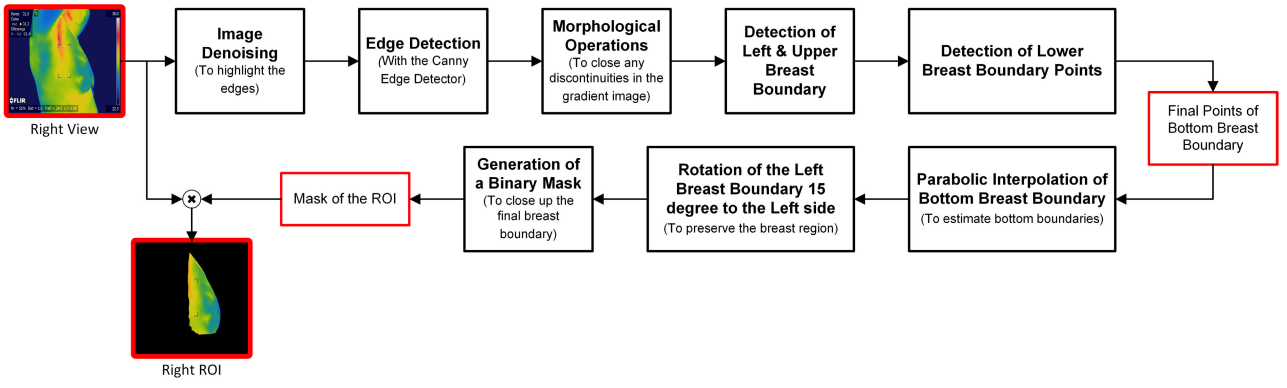

FIGURE 5. Block diagram of lateral breast thermogram segmentation method.

compared to a model that only uses a single input, thus forming a synergy of the sub-networks. This is because, during the training process, the weights of the sub-networks are updated based on the combined error by the training algorithm (i.e., back-propagation). By incorporating multi-inputs, the model can adjust the weights in a way that takes

Algorithm 1 Frontal Thermogram Segmentation

Data: I
Result: $I_{roi}, I_{left}, I_{right}$
$I_{grey} \leftarrow$ rgb2grey(I)
$I_{filtered} \leftarrow$ ADF(I_{grey})
$I_{edges} \leftarrow$ CannyEDetector($I_{filtered}, \sigma, \alpha$)
$I_{closed} \leftarrow I_{edges} \cdot S_{3\times3}$ {morphological closing}
$I_{dilated} \leftarrow I_{close} \oplus S_{3\times3}$ {morphological dilation}
$I_{nohole} \leftarrow$ FilterObjectsWithoutHoles($I_{dilated}$)
$C1 \leftarrow \varnothing$
$C2 \leftarrow \varnothing$
for c in I_{nohole} **do**
  if hasDarkpixels($I_{nohole}(c, r_{c,min} : r_{c,max})$) **then**
    $C1 \leftarrow c$
    break
  end if
end for
for c in I_{nohole} in reverse **do**
  if hasDarkpixels($I_{nohole}(c, r_{c,min} : r_{c,max})$) **then**
    $C2 \leftarrow c$
    break
  end if
end for
$R_u \leftarrow$ FindUpperBoundary($C1, C2$)
$R_{bottom}, C_{bottom} \leftarrow$ TraceLowerBoundary($C1, C2, R_{up}$)
$P_{left}, P_{right} \leftarrow$ fitPolynomials($R_{bottom}, C_{bottom}, 2$)
$r_{inter}, c_{inter} \leftarrow$ intersection(P_{left}, P_{right})
$I_{bound} \leftarrow$ closeFill($I_{grey}, P_{left}, P_{right}, R_u, r_{inter}, c_{inter}$)
$I_{mask} \leftarrow I_{bound}$
for r, c in I_{mask} **do**
  if intensity at $I_{mask}(r, c) \geq thresh$ **then**
    $I_{mask}(r, c) \leftarrow 1$
  else
    $I_{mask}(r, c) \leftarrow 0$
  end if
end for
$I_{roi} \leftarrow I_{mask} \otimes I$
$I_{left}, I_{right} \leftarrow imcrop(I_{roi}, r_{inter}, c_{inter})$

Algorithm 2 Lateral Thermogram Segmentation

Data: I
Result: I_{roi}
$I_{grey} \leftarrow$ rgb2grey(I)
$I_{filtered} \leftarrow$ ADF(I_{grey})
$I_{edges} \leftarrow$ CannyEDetector($I_{filtered}, \sigma, \alpha$)
$I_{closed} \leftarrow I_{edges} \cdot S_{3\times3}$ {morphological closing}
$I_{dilated} \leftarrow I_{close} \oplus S_{3\times3}$ {morphological dilation}
$r_n, c_n \leftarrow$ TraceUpperBoundary($I_{dilated}$)
for c in $I_{dilated}$ in reverse **do**
  if hasDarkpixels($I_{dilated}(c, r_{c,min} : r_{c,max})$) **then**
    $C_{bottom}, R_{bottom} \leftarrow getboundary(I_{dilated}(c_n : c, r_{c,max} : end))$
    break
  end if
end for
$P \leftarrow$ fitPolynomial($C_{bottom}, R_{bottom}, 2$)
$\theta \leftarrow -15°$
$c_{rot} \leftarrow (c_{old} - c_n)\cos\theta - (r_{old} - r_n)\sin\theta$
$r_{rot} \leftarrow (c_{old} - c_n)\sin\theta + (r_{old} - r_n)\cos\theta$
$c_{new} \leftarrow c_{rot} + c_n$
$r_{new} \leftarrow r_{rot} + r_n$
$r_{inter}, c_{inter} \leftarrow$ interSection($P, r_{new}, c_{new}, r_n, c_n$)
$I_{bound} \leftarrow$ closenFill($I_{grey}, P, r_{inter}, c_{inter}, r_n, c_n$)
$I_{mask} \leftarrow I_{bound}$
for r, c in I_{mask} **do**
  if intensity at $I_{mask}(r, c) \geq thresh$ **then**
    $I_{mask}(r, c) \leftarrow 1$
  else
    $I_{mask}(r, c) \leftarrow 0$
  end if
end for
$I_{roi} \leftarrow I_{mask} \otimes I$

TABLE 3. Range of random values for image augmentation parameters.

Transformation	Range of Random values
Scale	0.1 to 1
XTranslation	−0.3 to 0.3
YTranslation	−0.3 to 0.3
Rotation	−10° to 10°

into account the information from all of the inputs, leading to a more robust and accurate model. According to [36], hybrid DNNs can be highly efficient and possess greater robustness towards incomplete data sets when contrasted against a solely DNN-based deep learning approach. This view is supported by findings in [37] where a hybrid model was trained on unstructured clinical notes combined with structured data. The model outperformed other models that utilize either unstructured notes or structured data only. Deep learning models are robust against catastrophic interference, a phenomenon that occurs when NNs are unable to retain old information in the presence of new one [38].

1) TRANSFER LEARNING-BASED ARCHITECTURE

Training deep networks is computationally demanding, but transfer learning can help reduce the need to train new models from scratch. To accomplish this, the pre-trained layers of AlexNet were adapted for processing the thermograms, and a simple NN was applied to the clinical data. Fig. 6 illustrates a block diagram of the proposed network, composed of pre-trained and newly trainable layers. CNNs are examples of DNNs that exhibit superior performance in visual recognition tasks, specifically in classification. Their effectiveness is attributed to their physiologically-inspired working principle, which mimics the brain's visual cortex. The visual cortex analyzes sensory nerve impulses from the eyes [16] and responds to specific receptive field patterns, with increasing complexity as patterns propagate through subsequent neural structures [17]. In line with this principle, CNNs extract low-level features in their initial layers and increase complexity in subsequent layers. As a result, CNN forms the basis for many DNN architectures used in image classification. In this study, we adapt a pre-trained CNN-based DNN, AlexNet, for sub-networks designed for processing thermograms, while a simple NN is used for clinical data. AlexNet's shallow architecture makes it faster to train, especially when dealing with multi-input images. This allows the network to learn correlations between different thermograms and improve classification performance. Introduced in [40]. As illustrated in

Fig. 7, the architecture of the model, starts with an image input layer of either 224 × 224 × 3 or 227 × 227 × 3 dimensions. This layer is followed by five convolutional layers, which extract spatially localized features within the input image, such as edges, curves, and textures, via small learnable kernels. These convolutional layers are interspersed with five pooling layers, which serve to downsample the feature maps and reduce the dimensionality of the data, thus retaining the most relevant information. Additionally, the model employs the Rectified Linear Unit (ReLU) activation function, which introduces non-linearity into the model and helps to avoid the problem of exploding and vanishing gradient [36]. The final three layers of AlexNet are Fully Connected Layers (FCL), meaning that each neuron in a given layer is connected to every neuron in the preceding layer. These layers serve to perform high-level feature extraction by aggregating the information extracted by the earlier layers and making the final prediction. To address the issue of overfitting, AlexNet includes dropout layers that randomly drop out units during training to prevent the network from relying too heavily on any one specific feature [41]. By default, AlexNet is trained to output a probability vector corresponding to 1000 classes. To adapt the AlexNet architecture for binary classification, certain layers were modified by adjusting the output layer to generate a single scalar value instead of a probability vector that corresponds to the positive class. This adaptation allowed the model to be trained for the specific task of binary classification. The last fully connected layer (FCL8) of AlexNet for NET-A was replaced with a new FCL. The new FCL was configured with 2 neurons, and the Weight Learning Rate Factor (WLRF) and Bias L2 Factor (BL2F) were set to 1. For NET-B, each of the three inputs corresponded to a separate AlexNet, and all layers from the last FCL were replaced with an FCL consisting of 2 neurons, with WLRF and BL2F set to 10. These values were increased to update the weights in these layers more quickly as parallel inputs were being processed. The outputs from each fine-tuned AlexNet were combined via the concatenation layer. This layer was followed by an FCL with 10 neurons and a WLRF set to 1. Next came batch normalization and the ReLU activation function. Finally, the last FCL had 2 neurons and a WLRF set to 1. A softmax layer was used for all networks. NET-C had a structure similar to NET-B, but with an additional link at the concatenation layer for the NN. This is summarized in Table. 4.

2) MODEL TRAINING

The training process was conducted using a Stochastic Gradient Descent Momentum (SGDM) optimizer to minimize the discrepancy between the predicted and actual output. This discrepancy was computed using the categorical cross-entropy loss function, as defined in (6)

$$\mathcal{L}(\hat{P}|P) = -\sum_{i} P(i) \log \hat{P}(i) \tag{6}$$

where $\hat{P}$ is the predicted class distribution, P as the true class distribution, and $i \in [1, N]$. To examine the effect of each

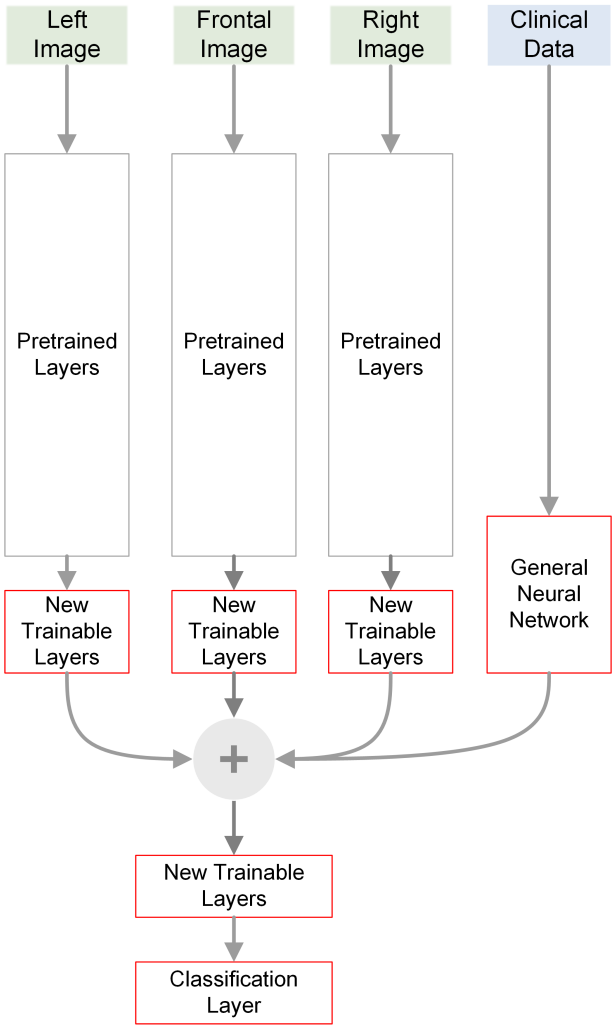

FIGURE 6. Schematic of the proposed transfer learning-based multi-input network architecture.

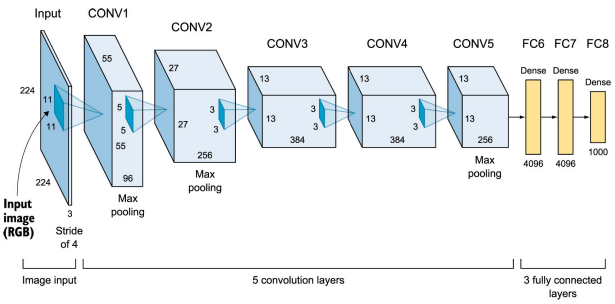

FIGURE 7. Block diagram of an AlexNet [39].

input, a network was first trained using only frontal thermograms and named NET-A. Then, lateral views were added to NET-A to form NET-B. Finally, NET-B was expanded by incorporating clinical data, to form NET-C. The training process was performed on a computer with an AMD Ryzen 5 3400G CPU (3.70 GHz), 16 GB of RAM, and an integrated Radeon Vega Graphics card. The experiments were executed on a MATLAB R2022b platform, utilizing the SGDM optimizer for training all models. The models used a momentum

TABLE 4. Comparison of NET-A, NET-B, and NET-C architectures.

Model	Inputs	No. AlexNet	Description
NET-A	Frontal Views	1	A simple AlexNet fine-tuned for binary classification. All layers from FCL8 are replaced with a FCL (2 neurons).
NET-B	All Views	3	Concatenation of 3 fine-tuned AlexNets, followed by FCL (10 neurons), batch normalization, ReLU activation, and another FCL (2 neurons). Each AlexNet has all layers from FCL8 replaced with an FCL (2 neurons).
NET-C	All Views & Clinical Data	3	Similar to NET-B but it also concatenates an additional link, of FCL (2 neurons) for clinical data.

parameter around 0.9, which is commonly used in SGDM optimization, to accelerate convergence and the stability of the optimization process. Moreover, the process was stabilized via l2norm regularization, which mitigates the issue of exploding gradients by clipping down the gradients [42]. The key hyperparameters and their configurations during the experiments are summarized in Table. 5.

F. EVALUATION CRITERION

1) PERFORMANCE EVALUATION OF SEGMENTATION METHOD

To validate the performance of the segmentation method, ground-truths for the ROI were manually created. These validated the proposed method through two standard and widely used image similarity metrics, the Dice Score and the Jaccard Index, defined in (7). These metrics provide an objective means to directly compare a manually generated ground-truth I_{gt} with the ROI extracted by the proposed method I_{exp} [43].

$$Jaccard\ coefficient: J\left(I_{gt}, I_{exp}\right) = \frac{\left|I_{gt} \cap I_{exp}\right|}{\left|I_{gt} \cup I_{exp}\right|} \tag{7}$$

$$Dice\ coefficient: D\left(I_{gt}, I_{exp}\right) = \frac{2 \cdot \left|I_{gt} \cdot I_{exp}\right|}{\left|I_{gt}\right| + \left|I_{exp}\right|} \tag{8}$$

Finally, the proposed approach was assessed for its sensitivity, precision, specificity, and accuracy, as specified by (9) to (12).

$$Accuracy = \frac{TP + TN}{TP + TN + FP + FN} \tag{9}$$

$$Precision = \frac{TP}{TP + FP} \tag{10}$$

$$Specificity = \frac{TN}{TN + FP} \tag{11}$$

$$Sensitivity = \frac{TP}{TP + FN} \tag{12}$$

where TN (True Negatives), FN (False Negative), TP (True Positive), and FP (False Positive).

TABLE 5. The configuration of hyperparameters employed during the training phase.

Hyperparameter	NET-A	NET-B	NET-C
Optimizer	SGFD	SGFD	SGFD
LearnRate	9×10^{-5}	5×10^{-4}	5×10^{-4}
MaxEpochs	8	8	8
MinBatchSize	32	32	32
L2Reularization	2.5×10^{-5}	1×10^{-4}	1×10^{-4}
GradientThresholdMethod	l2norm	l2norm	l2norm
Momentum	0.924	0.933	0.933

2) PERFORMANCE EVALUATION OF THE CLASSIFICATION MODEL

As already discussed in III-A, this study used a cohort of 100 (71 healthy and 29 sick) instances. The cohort was stratified and split into training, validation, and test sets in the ratios of 70%, 15%, and 15%, respectively. To balance the disparity between the two classes, the training set was augmented as a preventive measure against overfitting. In addition to metrics (9) to (12), an Area Under the Receiver Operator Curve (AUROC) was generated to visualize the model's degree of separability. These metrics were computed for three networks: one trained solely on frontal thermograms (NET-A), another trained on all thermograms (NET-B), and the overall network incorporating clinical data (NET-C). NET-C was compared with similar studies, as shown in Table. 8.

IV. RESULTS

A. SEGMENTATION RESULTS

The breast thermograms were segmented using a designated algorithm on each side. The images underwent denoising by applying a Gaussian filter with a standard deviation of $\sigma = 1.618$, followed by edge detection utilizing the Canny detector set to a threshold of $\alpha = 0.2333$. Fig. 8 shows segmented ROIs for three distinct instances. In each instance, the frontal ROI underwent a two-stage segmentation process, resulting in its extraction and bisection into the left and right breasts. This further division facilitates symmetry analysis. For each patient, the left and right ROIs are extracted from lateral views acquired at a 90-degree angle, which can also be used for symmetry analysis. Table. 6 demonstrates that the segmentation algorithm exhibited an average Jaccard index of 80.49% and an average Dice coefficient of 87.36% on frontal views. Conversely, the lateral view segmentation method achieved superior performance with an average Jaccard score of 85.7% and an average Dice coefficient of 92.01%.

B. CLASSIFICATION RESULTS

The illustration in Fig. 9 showcases a comprehensive directed acyclic graph for the network designated as NET-C. NET-A is structured as an AlexNet, with its terminal FCL optimized for binary classification. NET-B shares many similarities with NET-C but lacks the layers designed to handle clinical information. The outputs from the pre-trained and NN modules within NET-C are fused and fed into the latter part of the network to produce the global output. The dataset was partitioned into three portions: 70% for train-

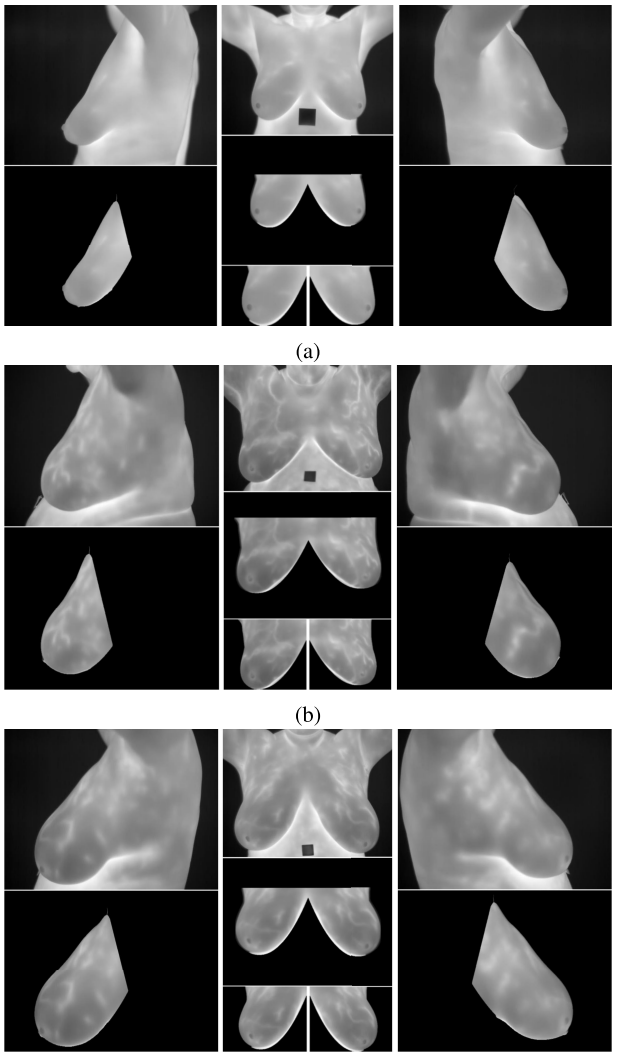

FIGURE 8. Illustration of original thermograms and their segmented ROIs. (a) Patient 1. (b) Patient 2. (c) Patient 3.

ing, 15% for validation, and 15% for testing. The training of the three models (NET-A, NET-B, and NET-C) resulted in test accuracy scores of 80.95%, 85.71%, and 90.48%. Fig. 10 depicts the accuracy and loss curves that showcase the performance of the models during the training process. It is worth noting that the training times for each model varied. Specifically, NET-A took 8 minutes 23 seconds to train, NET-B took 23 minutes 11 seconds, and NET-C took 23 minutes 2 seconds. These training times were relatively fast, and are indicative of the computational efficiency of the proposed method. Table. 7 shows the results of the three models on the test set. From these networks, it has been observed that the number of misclassified instances decreased as different inputs were factored in. The network trained only with frontal thermograms had four misclassifications, whereas using all views reduced this figure to 3. Utilizing both clinical data and all thermograms further decreased the number of misclassifications to 2. The performance of these classifiers can also be visualized via the ROC curves shown

TABLE 6. Performance metrics of the segmentation method.

Metric	Left Side	Right Side	Average on Lateral	Front Side
Jaccard Index	78.91 %	84.31 %	85.7 %	80.49 %
Dice Score	92.92 %	91.09 %	92.01 %	87.36 %
MCC	92.11 %	90.31 %	91.21 %	83.74 %
Accuracy	98.22 %	97.79 %	98.01 %	93.57 %
Sensitivity	94.28 %	93.22 %	93.75 %	90.39 %
Precision	92.24 %	90.51 %	91.39 %	86.08 %
Specificity	98.78 %	98.43 %	98.61 %	94.58 %

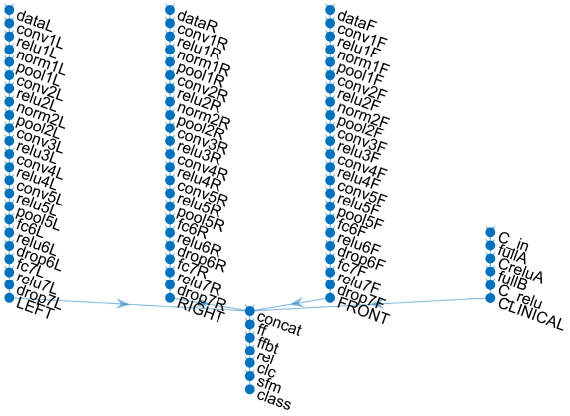

FIGURE 9. Directed acyclic graph for NET-C.

TABLE 7. Performances of the networks.

Model	Acc. (%)	Sen. (%)	Spec. (%)	Prec. (%)	AUROC	FN	FP
NET-A	80.95	93.33	50.00	82.35	0.93	1	3
NET-B	85.71	86.67	83.33	92.86	0.93	2	1
NET-C	90.48	93.33	83.33	93.33	0.94	1	1

in Fig. 11. These metrics demonstrate the model's capability to accurately distinguish sick patients from healthy ones and vice versa. Of the models tested, NET-C had the highest AUC of 0.94.

C. GRAPHIC USER INTERFACE

To demonstrate the functionality of the system, a GUI was developed using MATLAB's App Designer. The App seamlessly integrates the preprocessing and auto-segmentation methods for data preparation prior to feeding it into the model for prediction. This facilitated data transfer between the segmentation algorithm and the classification model. It also makes it possible to see the visual outputs of key steps, including gray-level histograms from contralateral breasts. Fig. 12 shows the GUI and the visual elements that appear during operation. Initially, a user uploads images and inputs relevant clinical information, as shown in Fig. 12(b). This is followed by preprocessing, in which the thermograms are segmented, and the resulting ROIs are displayed as shown in Fig. 12(c). The frontal ROI is further divided in half. The ROIs and clinical data are then fed into the model (in this case, NET-C), which provides the prediction score. Lastly, the user can generate and view the gray-level histograms of both breasts for symmetry analysis, as shown in Fig. 12(d).

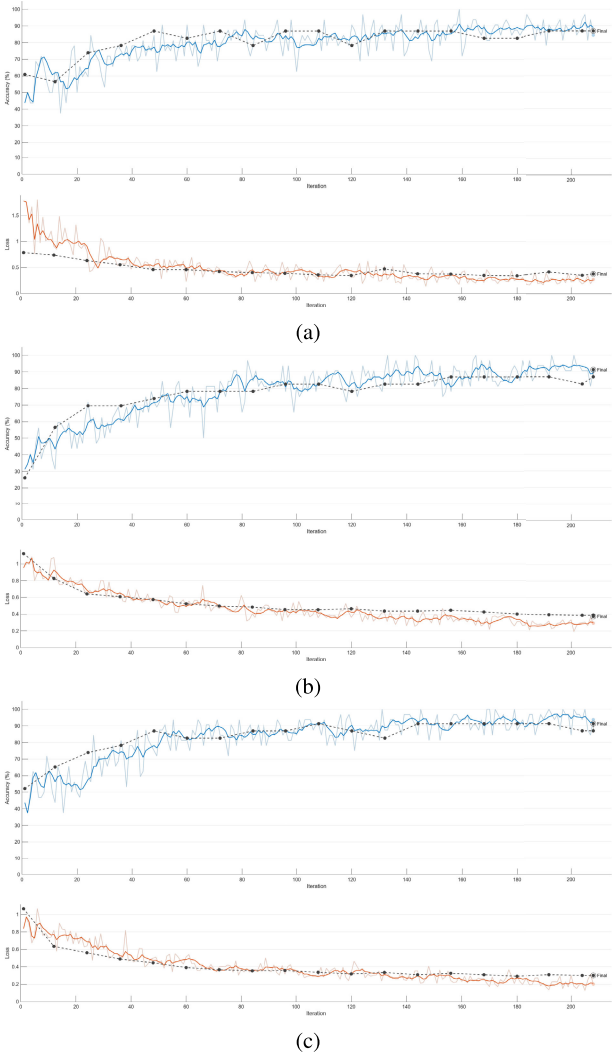

FIGURE 10. Training-validation loss and accuracy curves. (a) NET-A. (b) NET-B. (c) NET-C.

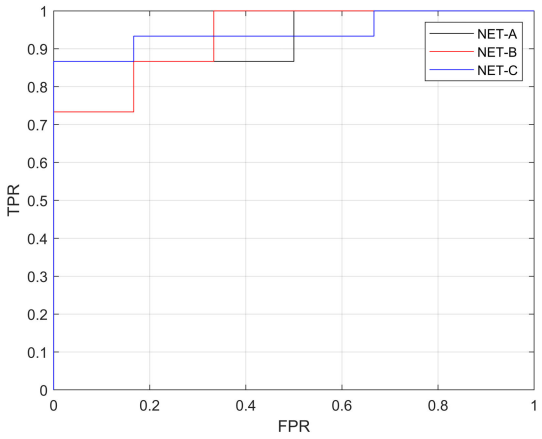

FIGURE 11. ROC curves for the test set.

V. DISCUSSION

In this study, a deep learning-based CADx system was proposed and assessed for breast cancer screening. The multi-input model demonstrated superiority over the conventional single-input model. Segmentation techniques for frontal and lateral breast thermograms were explored and evaluated. Results from the evaluation, as presented in Table. 6, indicate higher performance of the method for lateral thermograms compared to the one for frontal ones. This observation may be attributed to the more intricate shape and noise in some frontal images, and improper acquisition angles, which impeded the algorithm from performing an appropriate ROI extraction. However, consistent performance was observed between the lateral view segmentation algorithms. The ROIs were utilized for training three AlexNet-based models. The performance of these models on the test set is depicted in Table. 7. Model NET-A, which utilized only frontal thermograms, achieved an accuracy of 80.95% with four misclassifications. The addition of branches catering for left and right-view breast thermograms resulted in the formation of NET-B, leading to improved accuracy of 85.71% with three misclassifications. NET-C, an enhancement of NET-B that incorporates an extra layer for clinical data, achieved a 90.48% accuracy with only two misclassifications. The performance improvement is further demonstrated by the increase in the AUROC curve, as shown in Fig. 11, from 0.93 to 0.94, indicating the model's efficacy in classifying patients accurately as sick or healthy. The incorporation of lateral views demonstrated a significant reduction in number of FP. The integration of clinical data led to a decrease in FN compared to the previous model. These results concur with Sanchez et al.'s research [22], which highlights the benefits of incorporating clinical and personal information in reducing the number of FN. This implies that the inclusion of clinical and personal data enhances the efficacy of a CADx system.

The proposed model achieved a classification accuracy of 90.48%, which is lower than the accuracy reported in most related works presented in Table. 8. Notably, [22] achieved an accuracy of 97% using a similar dataset and identical views, but with twice the number of instances, while [25] attained a 93.8% accuracy using more instances and additional 45-degree acquired lateral views. The superior performance of these studies may be attributed to the larger number and greater diversity of instances in their datasets, which enable their models to learn more intricate features and patterns. Furthermore, two studies [24] and [44] that utilized DNNs outperformed the proposed model. These studies incorporated more advanced deep learning architectures, such as Inception V3 and VGG-16, that enable the capture of more complex features and patterns. The high performance of these studies could also be attributed to their use of effective preprocessing techniques, optimization algorithms, and a well-balanced dataset distribution.

Among all the studies listed, [46] demonstrated the best performance across all performance indicators. However, our proposed method offers several advantages over this study. Firstly, our proposed method uses a larger dataset, including 71 healthy and 29 sick individuals, compared to [46] that only used 35 normal and 28 abnormal cases. This larger dataset

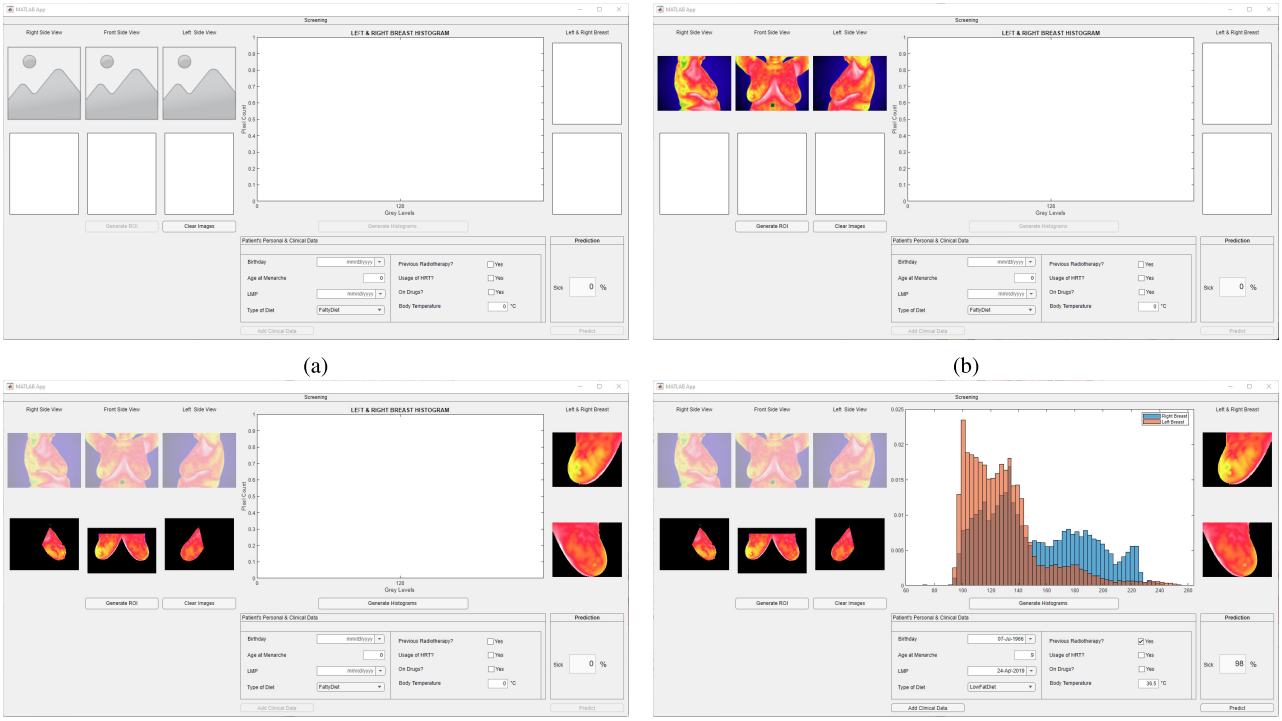

FIGURE 12. Illustration of key operations in the GUI during breast screening. (a) Original state. (b) Uploading of patient's information. (c) Information preprocessing. (d) Prediction and histogram generation.

TABLE 8. Comparison of the proposed work with similar approaches in literature.

Ref.	Model	Thermogram Sides	Dataset	Classes	Clinical Data	Seg.	Acc. (%)	Prec. (%)	Sens. (%)	Spec. (%)	AUROC
Ours	AlexNet	Front, Left-90°, and Right-90°	DMR-IR	101 (71 Healthy, 29 Sick)	Yes	Yes	90.48	93.33	93.33	83.33	0.94
[22]	CNN	Front, Left-90°, and Right-90°	DMR-IR	211 (170 healthy, 41 Sick)	Yes	No	97	–	83	100	0.99
[25]	CNN	Front, Left-90°, Left-45°, Rigt-90°, and Right-45°	DMR-IR	241 (157 Healthy, 84 Sick)	Yes	No	93.8	–	88.9	96.7	0.99
[23]	LS-SVM	Front, Left-90°, and Right-90°	DMR-IR	63 (32 Normal, 31 Abnormal)	No	No	96	100	100	92	0.96
[24]	VGG-16	Front, Left-90°, and Right-90°	DMR-IR	250 instances	No	No	98	98	98	98	–
[10]	CNN	Front, Left-90°, Left-45°, Rigt-90°, and Right-45°	DMR-IR	140 (98 Healthy, 42 Sick)	No	Yes	98.95	99.56	98.28	99.59	–
[44]	Inception V3	Front	DMR-IR	67 (43 healthy, 24 Sick)	No	No	98.5	100	97.5	–	–
[45]	MLP	Front	DMR-IR	155 (81 Normal, 74 abnormal)	No	No	90.9	92.8	90.6	91.3	0.94
[46]	CNN	Front	DMR-IR	63 (35 Normal, 28 Abnormal)	No	No	100	100	100	100	1

Sensitivity(Sen.), Specificity (Spec.), Precision (Prec.), Accuracy (Acc.)

provides a more comprehensive understanding of the pathology and better generalizability of the model. Moreover, our proposed method utilizes clinical data, which is essential for identifying specific characteristics of the pathology and significantly improves the model's performance. Secondly, our proposed method uses both frontal and lateral thermogram views, whereas [46] only uses frontal views. Lateral views can provide additional information that is not visible in frontal views which can enhance the sensitivity of the model. Despite the lower classification accuracy achieved by the proposed model, it is noteworthy that the model achieved a reasonably high accuracy despite the limitations of a small dataset and

class imbalance. Furthermore, the model's adaptability to small datasets with class imbalances makes it a practical and useful tool for breast cancer detection.

Although deep learning models have the potential to enhance performance, they necessitate more data for training, longer model training durations, and greater computational power compared to conventional machine learning algorithms [47], [48]. To address these drawbacks, this study integrated the transfer learning technique. As already highlighted, this involves utilizing a pre-trained model to transfer knowledge to a new, related task, which enables the model to learn faster and with fewer data points by reusing general features learned from the previous task. Through this technique, there was less training time, less complex computational infrastructure required, and fewer images were used compared to training a model from scratch. It took 23 minutes and 2 seconds to train NET-C, a process which could have elapsed for a far more duration if a new deep learning model was trained from scratch. Nevertheless, to achieve further advancements in performance, it may be necessary to employ a more advanced deep learning architecture and to consider pruning and quantization techniques, which can help address issues related to size and complexity. Additionally, a larger and better-balanced dataset may also lead to improved results. These findings emphasize the crucial role of incorporating multiple forms of data in the development of CADx systems for improved performance. Nonetheless, further validation is required through additional research, as this avenue has only been explored in limited studies.

VI. CONCLUSION

Breast cancer is a prevalent disease that affects women globally. The early detection of this disease is critical to improving patient outcomes and reducing mortality rates. This study presented a deep learning-based CADx system that incorporates multi-inputs, including frontal, right lateral, and left lateral breast thermograms, along with clinical data. The results reveal that as more inputs were integrated into the model, the number of FP and FN decreased, leading to an increase in accuracy. Specifically, an increase in accuracy was observed from 80.95% to 85.71% after adding lateral views, and a further improvement to 90.48% after incorporating clinical data. This offers valuable insights into the potential benefits of incorporating additional sources of data to enhance the performance of CADx systems. Implementing a GUI and auto-segmentation into the proposed framework greatly enhances the efficiency of the screening workflow. This is achieved by reducing the potential for human error and lowering computational demands since only ROIs are processed. Moreover, transfer learning leveraged in this study, lead to a more cost-effective training process which required only a small number of training samples and less computationally intensive hardware. This approach yielded a CADx model with high generalization ability, showcasing the efficacy of transfer learning. The proposed model was evaluated by comparing it to similar models in the literature on various performance indicators. While some related works performed better, it is worth noting that the proposed model achieved reasonable results on a small and imbalanced dataset, a common scenario for breast cancer detection. The proposed framework is not limited to breast cancer detection as it can be adapted to other medical imaging tasks. Additionally, it can potentially be applied in mass screening efforts. Overall, the study presented a promising step towards the application of computer vision techniques in medical radiology. Future research is necessary to validate and enhance the proposed model, and investigate the integration of additional data sources. These efforts will present an opportunity to advance the field of medical radiology and ultimately improve healthcare outcomes.

ACKNOWLEDGMENT

The authors would like to thank the financial support from Prince Sultan University for the payment of Article Processing Charges for this research work.

REFERENCES

[1] H. Sung, J. Ferlay, R. L. Siegel, M. Laversanne, I. Soerjomataram, A. Jemal, and F. Bray, "Global cancer statistics 2020: GLOBOCAN estimates of incidence and mortality worldwide for 36 cancers in 185 countries," *CA, Cancer J. Clinicians*, vol. 71, no. 3, pp. 209–249, May 2021.

[2] M. Bellanger, N. Zeinomar, P. Tehranifar, and M. B. Terry, "Are global breast cancer incidence and mortality patterns related to country-specific economic development and prevention strategies?" *J. Global Oncol.*, vol. 2018, no. 4, pp. 1–16, Dec. 2018.

[3] M. Macedo, M. Santana, W. P. D. Santos, R. Menezes, and C. Bastos-Filho, "Breast cancer diagnosis using thermal image analysis: A data-driven approach based on swarm intelligence and supervised learning for optimized feature selection," *Appl. Soft Comput.*, vol. 109, Sep. 2021, Art. no. 107533.

[4] R. A. D. C. Vieira, G. Biller, G. Uemura, C. A. Ruiz, and M. P. Curado, "Breast cancer screening in developing countries," *Clinics*, vol. 72, no. 4, pp. 244–253, 2017.

[5] F. Z. Francies, R. Hull, R. Khanyile, and Z. Dlamini, "Breast cancer in low-middle income countries: Abnormality in splicing and lack of targeted treatment options," *Amer. J. Cancer Res.*, vol. 10, no. 5, pp. 1568–1591, 2020.

[6] O. Ginsburg et al., "Breast cancer early detection: A phased approach to implementation," *Cancer*, vol. 126, no. S10, pp. 2379–2393, May 2020.

[7] C. Nickson and A. M. Kavanagh, "Tumour size at detection according to different measures of mammographic breast density," *J. Med. Screening*, vol. 16, no. 3, pp. 140–146, Sep. 2009.

[8] J. Amin, M. Sharif, S. L. Fernandes, S. Wang, T. Saba, and A. R. Khan, "Breast microscopic cancer segmentation and classification using unique 4-qubit-quantum model," *Microsc. Res. Technique*, vol. 85, no. 5, pp. 1926–1936, May 2022.

[9] M. J. Yaffe and J. G. Mainprize, "Risk of radiation-induced breast cancer from mammographic screening," *Radiology*, vol. 258, no. 1, pp. 98–105, Jan. 2011.

[10] S. Ekici and H. Jawzal, "Breast cancer diagnosis using thermography and convolutional neural networks," *Med. Hypotheses*, vol. 137, Apr. 2020, Art. no. 109542.

[11] M. Dykstra, B. Malone, O. Lekuntwane, J. Efstathiou, V. Letsatsi, S. Elmore, C. Castro, N. Tapela, and S. Dryden-Peterson, "Impact of community-based clinical breast examinations in Botswana," *JCO Global Oncol.*, no. 7, pp. 17–26, Dec. 2021.

[12] D. Singh and A. K. Singh, "Role of image thermography in early breast cancer detection-past, present and future," *Comput. Methods Programs Biomed.*, vol. 183, Jan. 2020, Art. no. 105074.

[13] G. Meenalochini and S. Ramkumar, "Survey of machine learning algorithms for breast cancer detection using mammogram images," *Mater. Today, Proc.*, vol. 37, pp. 2738–2743, Jan. 2021.

[14] A. A. Khan and A. S. Arora, "Thermography as an economical alternative modality to mammography for early detection of breast cancer," *J. Healthcare Eng.*, vol. 2021, pp. 1–8, Jul. 2021.

[15] R. Owen and S. Ramlakhan, "Infrared thermography in paediatrics: A narrative review of clinical use," *BMJ Paediatrics Open*, vol. 1, no. 1, pp. 1–10, 2017.

[16] C. Siu and K. Murphy, "The development of human visual cortex and clinical implications," *Eye Brain*, vol. 10, pp. 25–36, Apr. 2018.

[17] D. H. Hubel and T. N. Wiesel, "Receptive fields, binocular interaction and functional architecture in the cat's visual cortex," *J. Physiol.*, vol. 160, no. 1, pp. 106–154, Jan. 1962.

[18] W.-H. Choi and Y.-S. Choi, "Effective pre-training method and its compositional intelligence for image captioning," *Sensors*, vol. 22, no. 9, p. 3433, Apr. 2022.

[19] S. Mambou, P. Maresova, O. Krejcar, A. Selamat, and K. Kuca, "Breast cancer detection using infrared thermal imaging and a deep learning model," *Sensors*, vol. 18, no. 9, p. 2799, Aug. 2018.

[20] S. Dey, R. Roychoudhury, S. Malakar, and R. Sarkar, "Screening of breast cancer from thermogram images by edge detection aided deep transfer learning model," *Multimedia Tools Appl.*, vol. 81, no. 7, pp. 9331–9349, Mar. 2022.

[21] A. S. Elkorany, M. Marey, K. M. Almustafa, and Z. F. Elsharkawy, "Breast cancer diagnosis using support vector machines optimized by whale optimization and dragonfly algorithms," *IEEE Access*, vol. 10, pp. 69688–69699, 2022.

[22] R. Sánchez-Cauce, J. Pérez-Martín, and M. Luque, "Multi-input convolutional neural network for breast cancer detection using thermal images and clinical data," *Comput. Methods Programs Biomed.*, vol. 204, Jun. 2021, Art. no. 106045.

[23] V. Madhavi and C. B. Thomas, "Multi-view breast thermogram analysis by fusing texture features," *Quant. Infr. Thermogr. J.*, vol. 16, no. 1, pp. 111–128, Jan. 2019.

[24] D. Tiwari, M. Dixit, and K. Gupta, "Deep multi-view breast cancer detection: A multi-view concatenated infrared thermal images based breast cancer detection system using deep transfer learning," *Traitement Signal*, vol. 38, no. 6, pp. 1699–1711, Dec. 2021.

[25] M. J. Mammoottil, L. J. Kulangara, A. S. Cherian, P. Mohandas, K. Hasikin, and M. Mahmud, "Detection of breast cancer from five-view thermal images using convolutional neural networks," *J. Healthcare Eng.*, vol. 2022, pp. 1–15, Feb. 2022.

[26] L. F. Silva, D. C. M. Saade, G. O. Sequeiros, A. C. Silva, A. C. Paiva, R. S. Bravo, and A. Conci, "A new database for breast research with infrared image," *J. Med. Imag. Health Informat.*, vol. 4, no. 1, pp. 92–100, Mar. 2014.

[27] A. McGuire, J. Brown, C. Malone, R. McLaughlin, and M. Kerin, "Effects of age on the detection and management of breast cancer," *Cancers*, vol. 7, no. 2, pp. 908–929, May 2015.

[28] M. Goldberg, A. A. D'Aloisio, K. M. O'Brien, S. Zhao, and D. P. Sandler, "Pubertal timing and breast cancer risk in the sister study cohort," *Breast Cancer Res.*, vol. 22, no. 1, pp. 1–11, Dec. 2020.

[29] Collaborative Group on Hormonal Factors in Breast Cancer, "Menarche, menopause, and breast cancer risk: Individual participant meta-analysis, including 118 964 women with breast cancer from 117 epidemiological studies," *Lancet. Oncol.*, vol. 13, no. 11, pp. 1141–1151, Nov. 2012.

[30] M. R. Ataollahi, J. Sharifi, M. R. Paknahad, and A. Paknahad, "Breast cancer and associated factors: A review," *J. Med. Life*, vol. 8, no. 4, pp. 6–11, 2015.

[31] M. Michèle et al., "Dietary intake of trans fatty acids and breast cancer risk in 9 European countries," *BMC Med.*, vol. 19, no. 1, pp. 1–11, 2021.

[32] A. K. Ng and L. B. Travis, "Radiation therapy and breast cancer risk," *J. Nat. Comprehensive Cancer Netw.*, vol. 7, no. 10, pp. 1121–1128, 2009.

[33] Y. Vinogradova, C. Coupland, and J. Hippisley-Cox, "Use of hormone replacement therapy and risk of breast cancer: Nested case-control studies using the QResearch and CPRD databases," *BMJ*, vol. 371, Oct. 2020, Art. no. m3873.

[34] M. Steininger, K. Kobs, P. Davidson, A. Krause, and A. Hotho, "Density-based weighting for imbalanced regression," *Mach. Learn.*, vol. 110, no. 8, pp. 2187–2211, Aug. 2021.

[35] J. Fang, "A critical review of five machine learning-based algorithms for predicting protein stability changes upon mutation," *Briefings Bioinf.*, vol. 21, no. 4, pp. 1285–1292, Jul. 2020.

[36] V. Gavrishchaka, Z. Yang, R. Miao, and O. Senyukova, "Advantages of hybrid deep learning frameworks in applications with limited data," *Int. J. Mach. Learn. Comput.*, vol. 8, no. 6, pp. 549–558, Dec. 2018.

[37] D. Zhang, C. Yin, J. Zeng, X. Yuan, and P. Zhang, "Combining structured and unstructured data for predictive models: A deep learning approach," *BMC Med. Informat. Decis. Making*, vol. 20, no. 1, pp. 1–11, Dec. 2020.

[38] P. Kaushik, A. Gain, A. Kortylewski, and A. Yuille, "Understanding catastrophic forgetting and remembering in continual learning with optimal relevance mapping," 2021, *arXiv:2102.11343*.

[39] M. Elgendy, *Deep Learning for Vision Systems*, 1st ed. Shelter Island, NY, USA: Manning Publications, 2020.

[40] A. Krizhevsky, I. Sutskever, and G. E. Hinton, "ImageNet classification with deep convolutional neural networks," in *Advances in Neural Information Processing Systems*, vol. 25, F. Pereira, C. J. Burges, L. Bottou, and K. Q. Weinberger, Eds. Red Hook, NY, USA: Curran Associates, 2012.

[41] S. Han, F. Yang, G. Yang, B. Gao, N. Zhang, and D. Wang, "Electrical equipment identification in infrared images based on ROI-selected CNN method," *Electr. Power Syst. Res.*, vol. 188, Nov. 2020, Art. no. 106534.

[42] X. Chen, Z. S. Wu, and M. Hong, "Understanding gradient clipping in private SGD: A geometric perspective," in *Proc. Adv. Neural Inf. Process. Syst.*, Dec. 2020, pp. 1–31.

[43] A. Klein, S. Falkner, S. Bartels, P. Hennig, and F. Hutter, "Fast Bayesian optimization of machine learning hyperparameters on large datasets," in *Proc. 20th Int. Conf. Artif. Intell. Statist. (AISTATS)*, vol. 54, 2017, pp. 528–536.

[44] S. S. Yadav and S. M. Jadhav, "Thermal infrared imaging based breast cancer diagnosis using machine learning techniques," *Multimedia Tools Appl.*, vol. 81, no. 10, pp. 13139–13157, Apr. 2022.

[45] S. Pramanik, D. Bhattacharjee, and M. Nasipuri, "MSPSF: A multi-scale local intensity measurement function for segmentation of breast thermogram," *IEEE Trans. Instrum. Meas.*, vol. 69, no. 6, pp. 2722–2733, Jun. 2020.

[46] S. Tello-Mijares, F. Woo, and F. Flores, "Breast cancer identification via thermography image segmentation with a gradient vector flow and a convolutional neural network," *J. Healthcare Eng.*, vol. 2019, pp. 1–13, Nov. 2019.

[47] A. Varghese, G. Agyeman-Badu, and M. Cawley, "Deep learning in automated text classification: A case study using toxicological abstracts," *Environ. Syst. Decis.*, vol. 40, pp. 465–479, Feb. 2020.

[48] V. S. Nori, C. A. Hane, Y. Sun, W. H. Crown, and P. A. Bleicher, "Deep neural network models for identifying incident dementia using claims and EHR datasets," *PLoS ONE*, vol. 15, no. 9, Sep. 2020, Art. no. e0236400.

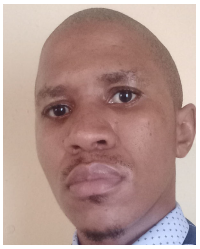

DENNIES TSIETSO (Student Member, IEEE) received the B.Eng. degree in computer and telecommunications from the Botswana International University of Science and Technology, in 2020, where he is currently pursuing the M.Eng. degree in computer and telecommunications. He is a Registered Graduate Engineer with the Engineers Registration Board, which regulates the engineering profession in Botswana. His research interests include image processing, machine learning, and deep learning, with a focus on developing novel algorithms for image classification and recognition. His academic achievements, professional registrations, and research interests demonstrate his commitment to becoming an expert in computer engineering and his passion for innovation and problem-solving.

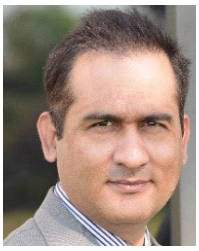

ABID YAHYA (Senior Member, IEEE) received the bachelor's degree in electrical and electronic engineering and in telecommunication from the University of Engineering and Technology Peshawar, Peshawar, Pakistan, and the M.Sc. and Ph.D. degrees in wireless and mobile systems from Universiti Sains Malaysia. He is currently with the Botswana International University of Science and Technology, which has employed him because of his practical knowledge and educational experience to aid them in many consulting jobs for giant enterprises. He is a Professional Engineer certified by the Botswana Engineers Registration Board (ERB). In addition to having more than 140 publications in renowned journals, conferences, and books, he has received numerous awards and grants from multiple funding sources. Additionally, he has taught countless master's and Ph.D. degree students. Universities all over the country and around the world study his books.

RAVI SAMIKANNU (Senior Member, IEEE) received the Ph.D. degree in electrical engineering from Anna University, India, in 2012. He is currently an Associate Professor with the Department of Electrical Computer and Telecommunications Engineering, Botswana International University of Science and Technology, Botswana. He has a total teaching experience of 18 years. At present, four Ph.D. and five master's students are doing research under his supervision, and three Ph.D. students and 19 master's students completed their research work under his supervision. He has published more than 100 research articles in journals and presented 70 papers in conferences. He is also working on smart grid, digital electronics, power systems, and power electronics.

MUHAMMAD USMAN TARIQ (Member, IEEE) is currently an Associate Professor with Abu Dhabi University, Abu Dhabi Campus. Previously, he has held various academic and leadership appointments over the past 15 years in industry and academia. He has been a consultant, a master trainer, and an assessor for local and international organizations. He has diverse and significant experience working with accreditation agencies of ABET, ACBSP, AACSB, WASC, CAA, EFQM, AMBA, BGA, and NCEAC. Additionally, he has operational expertise in incubators, research laboratories, government research projects, case centers, private sector startups, program creation, and management at various industrial and academic levels. He is a Certified Higher Education Teacher with Harvard University, USA, the Certified Change Leader, and an Assessor with EFQM Brussels, CIPD Level 7 SRLD Certified, a Certified Online Educator with HMBSU, Certified Six Sigma Master Black Belt, and a Lead Auditor of ISO 9001 Certified, ISO 14001, IOSH MS, OSHA 30, and OSHA 48. He has been awarded a Certified Chartered Fellowship from CIPD U.K. He holds professional memberships with IEEE, APPAM, and ACM.

MUHAMMAD BABAR (Member, IEEE) received the Master of Science and Ph.D. degrees in computer software engineering from the National University of Sciences and Technology (NUST), Islamabad, Pakistan, in 2018. He is currently with Prince Sultan University (PSU), Saudi Arabia. His research interests include but are not limited to big data analytics, machine learning, the Internet of Things (IoT), smart city design and planning, security, and the social web of things (SWOT). He has published his research work in various IEEE, Elsevier, and Springer journals. He actively reviews *FGCS* (Elsevier), *MONET* (Springer), *Computer Networks* (Elsevier), IEEE Access, *Heliyon* (Elsevier), and *Transactions on Emerging Telecommunications Technologies* (Wiley). He has been a part of the technical program committee of various conferences and workshops. He has also edited several special issues as a guest editor in leading journals.

BASIT QURESHI (Senior Member, IEEE) received the bachelor's degree in computer science from Ohio University, Athens, OH, USA, in 2000, the master's degree in computer science from Florida Atlantic University, in 2002, and the Ph.D. degree in computer science from the University of Bradford, U.K., in 2011. He is currently an Associate Professor and the Chair of the Department of Computer Science, Prince Sultan University, Saudi Arabia. He has published over 60 research works in the area of robotics, the Internet of Things, machine learning, and computational intelligence. He is a member of the IEEE Computer Society, the IEEE Communications Society, and the ACM.

ANIS KOUBAA (Senior Member, IEEE) is currently a Professor in computer science and the Leader of the Robotics and Internet of Things Research Laboratory, Prince Sultan University. He is also a Senior Researcher with CISTER and ISEP-IPP, Porto, Portugal, and a Research and Development Consultant with Gaitech Robotics, China. His current research interests include providing solutions for the integration of robots and drones into the Internet of Things (IoT) and clouds in the context of cloud robotics, robot operating systems (ROSs), robotic software engineering, wireless communication for the IoT, real-time communication, safety and security for cloud robotics, intelligent algorithm's design for mobile robots, and multi-robot task allocation. He is also a Senior Fellow of the Higher Education Academy (HEA), U.K. He has been the Chair of the ACM Chapter in Saudi Arabia, since 2014.